Biophysical *Journal*
Biophysical Letter

Biophysical Society

Direct Observation of Cell-Cycle-Dependent Interactions between CTCF and Chromatin

Harsha Agarwal,[1] Matthias Reisser,[1] Celina Wortmann,[1] and J. Christof M. Gebhardt[1,*]
[1]Institute of Biophysics, Ulm University, Ulm, Germany

ABSTRACT The three-dimensional arrangement of chromatin encodes regulatory traits important for nuclear processes such as transcription and replication. Chromatin topology is in part mediated by the architectural protein CCCTC-binding factor (CTCF) that binds to the boundaries of topologically associating domains. Whereas sites of CTCF interactions are well characterized, little is known on how long CTCF binds to chromatin and how binding evolves during the cell cycle. We monitored CTCF-chromatin interactions by live cell single molecule tracking in different phases of the cell cycle. In G1-, S-, and G2-phases, a majority of CTCF molecules was bound transiently (∼0.2 s) to chromatin, whereas minor fractions were bound dynamically (∼4 s) or stably (>15 min). During mitosis, CTCF was mostly excluded from chromatin. Our data suggest that CTCF scans DNA in search for two different subsets of specific target sites and provide information on the timescales over which topologically associating domains might be restructured. During S-phase, dynamic and stable interactions decreased considerably compared to G1-phase, but were resumed in G2-phase, indicating that specific interactions need to be dissolved for replication to proceed.

Chromatin exhibits architectural traits ranging from the state of compaction by nucleosomes over DNA loops and topologically associating domains (TADs) to the relative location of whole chromosomes (1,2). Chromatin topology contributes to the orchestration of vital nuclear tasks such as gene transcription by regulating enhancer and promoter contacts (3) or DNA replication, condensation, and repair (4–6). A rich variety of biomolecules involved in organizing the genome has been identified, including nuclear lamina, noncoding RNA, and architectural proteins such as cohesin and condensin. Recently, the evolutionary conserved transcription factor CTCF emerged to have fundamental roles in organizing chromatin architecture (7,8). CTCF functions are associated with gene activation and repression, enhancer-promoter insulation, and separation of chromatin domains, most of which can be attributed to its general role as "master weaver" of chromatin topology (9).

Interphase chromatin is dynamic and exhibits local and long-range movements (10), thereby enabling functional contacts to be initiated and rearranged. For example, rearrangements of the MHC-II locus happen within the first 30 min after upregulation of gene expression by interferon-γ (11). Compatible with dynamic rearrangements, estimates of the dynamical behavior of CTCF and other architectural proteins by fluorescence recovery after photobleaching experiments revealed recovery times on the order of seconds to minutes (12–14). However, detailed interaction times of architectural proteins with chromatin that would report on their ability to fix chromatin structures over time are missing, leaving questions central to a mechanistic understanding of chromatin organization unanswered.

To observe CTCF in living cells, we created WI-38 cell lines expressing a HaloTag-CTCF fusion protein (Halo-CTCF) from a doxycycline-inducible promoter (Supporting Materials and Methods). 24 h before the experiments, we added 5 ng/μL doxycycline to ensure low Halo-CTCF expression comparable to endogenous CTCF levels as quantified by Western blot and flow cytometry (Fig. S1; Supporting Materials and Methods). Notably, high Halo-CTCF expression led to accumulation of cells in S-phase, consistent with inhibition of cell growth by high CTCF concentrations (Fig. S2) (15). We transiently transfected the cells with RFP-cdt1 and GFP-geminin to distinguish among G1-phase, early S-phase (S-phase), or late S-/G2-phase (G2-phase) (16). Cells in M-phase were identified by staining DNA with Hoechst 33342. We visualized single SiR-labeled Halo-CTCF molecules (SiR-Halo-CTCF) (17) by inclined illumination on a custom-built microscope (Supporting Materials and Methods). Free SiR dye was efficiently removed during wash steps (Movie S1). In G1-, S-, and G2-phases, we could observe diffusing as well as bound SiR-Halo-CTCF molecules in the nucleus, revealing diverse

Submitted January 27, 2017, and accepted for publication April 14, 2017.
*Correspondence: christof.gebhardt@uni-ulm.de
Editor: Antoine van Oijen.
http://dx.doi.org/10.1016/j.bpj.2017.04.018

and widespread interaction kinetics of CTCF with chromatin (Fig. S3; Movies S2, S3, and S4). In contrast, CTCF was excluded from chromatin in M-phase, with only a few molecules interacting at various timescales (Fig. S4; Movie S5).

We characterized the binding times and number of interaction states between CTCF and chromatin in G1-, S-, and G2-phases by monitoring the fluorescent on-times of individual SiR-Halo-CTCF molecules using time-lapse illumination with different dark times (Fig. S5; Supporting Materials and Methods) (18). First, we determined the effective rate constant as a function of the time-lapse time by fitting a single-exponential decay model to each on-time histogram (Fig. S6). This approach is very sensitive toward the number of distinct dissociation rate constants of the protein (18) and suggested three interaction states for CTCF (Supporting Materials and Methods). We therefore next determined the values of the dissociation rate constants by globally fitting a triexponential decay model to the fluorescent on-time histograms (Fig. S5; Supporting Materials and Methods). Slow movements of chromatin or cells prevented unambiguous identification of molecules after very long dark times and limited determining the lowest dissociation rate constant. We therefore fixed this rate constant to an upper bound of 10^{-3}/s, as below this value the quality of the fit did not change considerably (Fig. S7).

Overall, our analysis revealed that interactions between CTCF and chromatin were grouped into three main regimes (Fig. 1 *A*). A majority (>80%) of CTCF molecules bound transiently to chromatin with a residence time of 0.2–0.6 s, whereas minor fractions bound dynamically with residence times of 4–8 s or were stable for >1000 s, respectively. The binding times and fractions of CTCF molecules at different cell cycle phases are summarized in Table S1. We observed significant differences in the frequencies of CTCF molecules in each of the interaction states (Fig. 1 *B*). The fraction of stable bound CTCF molecules decreased by more than a factor of 10 from G1- to S-phase, but recovered in G2-phase and exceeded the value in G1-phase by a factor of four. We found a similar, albeit less pronounced change for the dynamically bound fraction of CTCF. In contrast, the transiently bound fraction increased during S-phase and decreased in G2-phase compared to G1-phase.

To characterize whether the overall associations of CTCF to chromatin changed over the course of the cell cycle, we quantified the percentage of all bound SiR-Halo-CTCF molecules by measuring the distribution of step distances of SiR-Halo-CTCF in G1-, S-, and G2-phases (Fig. S8) (18), or by comparing intensities adjacent to and colocalizing with chromatin in M-phase (Supporting Materials and Methods). We observed a small decrease of bound CTCF molecules from G1- to G2-phase and a strong drop in M-phase (Fig. 1 *B*, *left inset* and Table S1).

The shortest CTCF-chromatin interaction time is comparable to a transient binding state that has been observed in addition to longer binding events for many DNA binding proteins in single molecule tracking experiments (19–23). Several independent studies identified the class of transient interactions as interactions with DNA sequences unspecific for the transcription factor (23–25), whereas longer binding events in the range of seconds were associated with binding of the transcription factor to specific target sites (19–23). We thus suppose that the major fraction of transiently binding CTCF molecules associate to unspecific DNA sequences for short times in search for specific CTCF target sequences (Fig. 2).

The remaining two binding populations of CTCF exhibit binding times in the range of seconds and minutes, pointing to interactions with specific DNA sequences with divergent binding affinity. In the genome, ~100,000 CTCF binding sites have been identified (26), most of which are located at TAD boundaries (27,28), but also within TADs (27,29). CTCF binding sites have been categorized into different classes

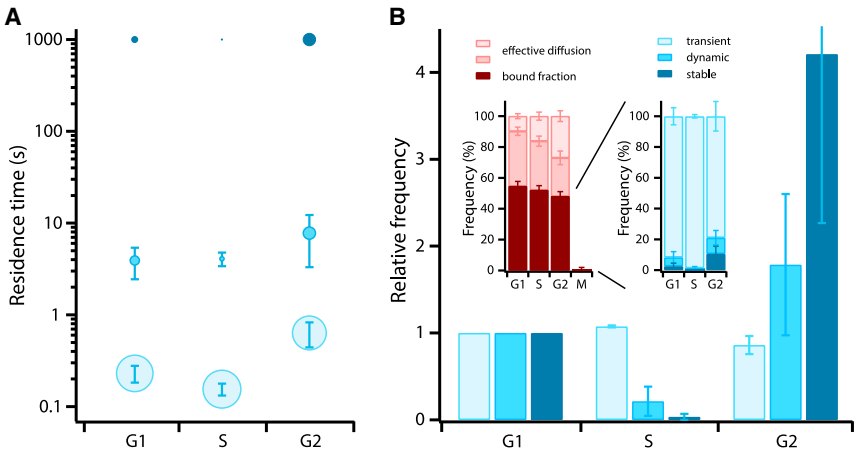

FIGURE 1 Comparison of residence times and frequencies of SiR-Halo-CTCF-chromatin interactions between different cell cycle phases. (*A*) Shown here are chromatin residence times of SiR-Halo-CTCF in G1-, S-, and G2-phases. The symbol area is proportional to the fraction of molecules exhibiting the corresponding binding time. Error bars denote SD. (*B*) Shown here are relative frequencies of SiR-Halo-CTCF molecules exhibiting transient (*light blue*), dynamic (*blue*), and stable (*dark blue*) interactions with chromatin in S- and G2-phases compared to G1-phase. (*Left inset*) Shown here are fractions of molecules bound to chromatin (*dark red*) and of molecules exhibiting effective diffusion (*red and light red*). (*Right inset*) Shown here are fractions of molecules exhibiting transient (*light blue*), dynamic (*blue*), and stable (*dark blue*) interactions with chromatin in G1-, S-, and G2-phases. Error bars denote SD. To see this figure in color, go online.

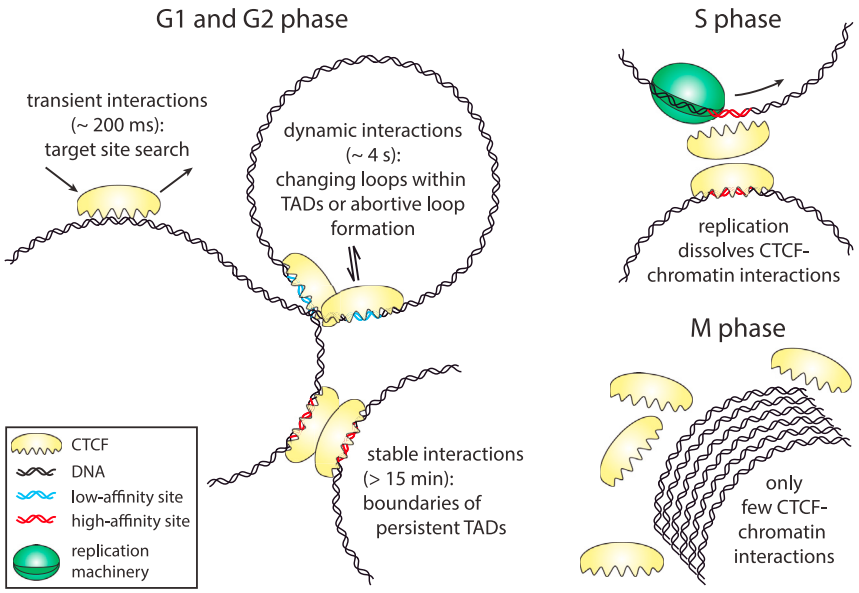

FIGURE 2 Shown here is a model of cell-cycle-dependent CTCF-chromatin interactions. To see this figure in color, go online.

based on divergent chromatin immune-precipitation occupancy scores (30,31). This is consistent with differential usage of CTCF zinc finger domains in recognizing different binding sites (14,32–34) and mediating orientational binding to different sequences (35). Low and high chromatin immune-precipitation occupancy sites could be identified with CTCF target sites of lower and higher binding affinity in in vitro experiments (36). Whereas low-affinity sites tend to be cell-type specific and are associated with high levels of gene expression, high-affinity sites are more conserved (30,36,37), reminiscent of the characteristics of loop structures within TADs and of the embracing TAD, respectively (29,38). Indeed, a correlation between conserved chromatin domain structures and high CTCF motive affinity was revealed in a comparison of chromatin structures between species (29,39). The dynamic CTCF-chromatin interactions we observed thus might represent interactions with low-affinity CTCF binding sites within TADs, whereas stable CTCF binding events might constitute interactions with high-affinity sites at TAD boundaries (Fig. 2).

This association is in line with the suggestion that DNA loops within TADs are mobile and changing, whereas the embracing TADs tend to be static and persistent during the cell cycle (1). Our model is also compatible with recently proposed loop extrusion models (40,41) in which stably occupied TAD boundaries would allow for efficient TAD formation, whereas dynamically bound CTCF would enable changing loop structures in nested TADs. Alternatively, dynamic interactions might reflect abortive loop or TAD formation. Future experiments will be necessary to unambiguously associate the CTCF interaction states to underlying chromatin structures. Nevertheless, within this model, our measurements provide information on the timescales over which the organizational features of chromatin might be restructured.

The timing of replication initiation in S-phase is intimately linked to chromatin topology, as TADs define the borders of early and late replication (42). This suggests that chromatin topology is to some extent maintained during S-phase, consistent with cell cycle-dependent Hi-C experiments (6). Intriguingly, we observed a significant decrease of specific CTCF-chromatin interactions in S- compared to G1-phase. Because overexpression of CTCF, which increases the absolute number of bound molecules, led to accumulation of cells in S-phase, dissolution of stable bound CTCF molecules seems to be necessary for undisturbed progression of the cell into G2-phase. We thus propose that competitive binding of CTCF and the replication machinery dissolves CTCF-chromatin interactions (Fig. 2). An analogous situation occurs in the regulation of splicing where bound CTCF slows down RNA polymerase II (43).

In G2-phase, dynamic and stable CTCF-chromatin interactions were resumed and added up to a fraction of ~20%. Whether these associations provoke a chromatin architecture comparable to G1-phase is unclear, because chromatin topology significantly changes during the transition from S- to M-phase (6). It is also controversial whether CTCF stays bound during mitosis (44,45). We found that CTCF was predominantly excluded from chromatin in M-phase, with only a few interacting molecules (Fig. 2).

Further elucidating the functional implications of CTCF-chromatin interaction kinetics and the role of CTCF in mediating chromatin topology during the cell cycle will be important future tasks.

SUPPORTING MATERIAL

Supporting Materials and Methods, eight figures, one table, and five movies are available at http://www.biophysj.org/biophysj/supplemental/S0006-3495(17)30434-4.

AUTHOR CONTRIBUTIONS

J.C.M.G. conceived the study. M.R. constructed the single molecule microscope. H.A. and J.C.M.G. designed the experiments. H.A. and C.W. performed the experiments. H.A., M.R., C.W., and J.C.M.G. analyzed data. J.C.M.G. wrote the manuscript with contributions from all authors.

ACKNOWLEDGMENTS

We thank Stefanie Weber for cloning the Halo-CTCF construct, Anja Palmer for support with single molecule microscopy, and Kai Johnsson (École Polytechnique Fédérale de Lausanne, Switzerland) for providing SiR dye.

This work was supported by the European Research Council (ERC) under the European Union's Horizon 2020 Research and Innovation Program (No. 637987 ChromArch to J.C.M.G.), the German Research Foundation (No. GE 2631/1-1 to J.C.M.G.), the German Academic Scholarship Foundation (to M.R.), and the DFG Graduate School of Molecular Medicine at Ulm University (to H.A.).

SUPPORTING CITATIONS

References (46–48) appear in the Supporting Material.

REFERENCES

1. Gibcus, J. H., and J. Dekker. 2013. The hierarchy of the 3D genome. *Mol. Cell.* 49:773–782.
2. Cremer, T., and M. Cremer. 2010. Chromosome territories. *Cold Spring Harb. Perspect. Biol.* 2:a003889–a003889.
3. Marsman, J., and J. A. Horsfield. 2012. Long distance relationships: enhancer-promoter communication and dynamic gene transcription. *Bioch. Biophys. Acta.* 1819:1217–1227.
4. Smith, O. K., and M. I. Aladjem. 2014. Chromatin structure and replication origins: determinants of chromosome replication and nuclear organization. *J. Mol. Biol.* 426:3330–3341.
5. Misteli, T., and E. Soutoglou. 2009. The emerging role of nuclear architecture in DNA repair and genome maintenance. *Nat. Rev. Mol. Cell Biol.* 10:243–254.
6. Naumova, N., M. Imakaev, …, J. Dekker. 2013. Organization of the mitotic chromosome. *Science.* 342:948–953.
7. Ohlsson, R., M. Bartkuhn, and R. Renkawitz. 2010. CTCF shapes chromatin by multiple mechanisms: the impact of 20 years of CTCF research on understanding the workings of chromatin. *Chromosoma.* 119:351–360.
8. Ong, C.-T., and V. G. Corces. 2014. CTCF: an architectural protein bridging genome topology and function. *Nat. Rev. Genet.* 15:234–246.
9. Phillips, J. E., and V. G. Corces. 2009. CTCF: master weaver of the genome. *Cell.* 137:1194–1211.
10. Hübner, M. R., and D. L. Spector. 2010. Chromatin dynamics. *Annu. Rev. Biophys.* 39:471–489.
11. Volpi, E. V., E. Chevret, …, D. Sheer. 2000. Large-scale chromatin organization of the major histocompatibility complex and other regions of human chromosome 6 and its response to interferon in interphase nuclei. *J. Cell Sci.* 113:1565–1576.
12. Gerlich, D., T. Hirota, …, J. Ellenberg. 2006. Condensin I stabilizes chromosomes mechanically through a dynamic interaction in live cells. *Curr. Biol.* 16:333–344.
13. Gerlich, D., B. Koch, …, J. Ellenberg. 2006. Live-cell imaging reveals a stable cohesin-chromatin interaction after but not before DNA replication. *Curr. Biol.* 16:1571–1578.
14. Nakahashi, H., K.-R. K. Kwon, …, R. Casellas. 2013. A genome-wide map of CTCF multivalency redefines the CTCF code. *Cell Reports.* 3:1678–1689.
15. Rasko, J. E. J., E. M. Klenova, …, V. V. Lobanenkov. 2001. Cell growth inhibition by the multifunctional multivalent zinc-finger factor CTCF. *Cancer Res.* 61:6002–6007.
16. Sakaue-Sawano, A., H. Kurokawa, …, A. Miyawaki. 2008. Visualizing spatiotemporal dynamics of multicellular cell-cycle progression. *Cell.* 132:487–498.
17. Lukinavičius, G., K. Umezawa, …, K. Johnsson. 2013. A near-infrared fluorophore for live-cell super-resolution microscopy of cellular proteins. *Nat. Chem.* 5:132–139.
18. Gebhardt, J. C. M., D. M. Suter, …, X. S. Xie. 2013. Single-molecule imaging of transcription factor binding to DNA in live mammalian cells. *Nat. Methods.* 10:421–426.
19. Chen, J., Z. Zhang, …, Z. Liu. 2014. Single-molecule dynamics of enhanceosome assembly in embryonic stem cells. *Cell.* 156:1274–1285.
20. Groeneweg, F. L., M. E. van Royen, …, M. J. M. Schaaf. 2014. Quantitation of glucocorticoid receptor DNA-binding dynamics by single-molecule microscopy and FRAP. *PLoS One.* 9:e90532.
21. Knight, S. C., L. Xie, …, R. Tjian. 2015. Dynamics of CRISPR-Cas9 genome interrogation in living cells. *Science.* 350:823–826.
22. Sugo, N., M. Morimatsu, …, N. Yamamoto. 2015. Single-molecule imaging reveals dynamics of CREB transcription factor bound to its target sequence. *Sci. Rep.* 5:10662.
23. Morisaki, T., W. G. Müller, …, J. G. McNally. 2014. Single-molecule analysis of transcription factor binding at transcription sites in live cells. *Nat. Commun.* 5:4456.
24. Caccianini, L., D. Normanno, …, M. Dahan. 2015. Single molecule study of non-specific binding kinetics of LacI in mammalian cells. *Faraday Discuss.* 184:393–400.
25. Ball, D. A., G. D. Mehta, …, T. S. Karpova. 2016. Single molecule tracking of Ace1p in *Saccharomyces cerevisiae* defines a characteristic residence time for non-specific interactions of transcription factors with chromatin. *Nucleic Acids Res.* 44:e160.
26. Kim, T. H., Z. K. Abdullaev, …, B. Ren. 2007. Analysis of the vertebrate insulator protein CTCF-binding sites in the human genome. *Cell.* 128:1231–1245.
27. Dixon, J. R., S. Selvaraj, …, B. Ren. 2012. Topological domains in mammalian genomes identified by analysis of chromatin interactions. *Nature.* 485:376–380.
28. Rao, S. S. P., M. H. Huntley, …, E. L. Aiden. 2014. A 3D map of the human genome at kilobase resolution reveals principles of chromatin looping. *Cell.* 159:1665–1680.
29. Tang, Z., O. J. Luo, …, Y. Ruan. 2015. CTCF-mediated human 3D genome architecture reveals chromatin topology for transcription. *Cell.* 163:1611–1627.
30. Essien, K., S. Vigneau, …, S. Hannenhalli. 2009. CTCF binding site classes exhibit distinct evolutionary, genomic, epigenomic and transcriptomic features. *Genome Biol.* 10:R131.
31. Fang, R., C. Wang, …, Z. Zhang. 2015. Functional diversity of CTCFs is encoded in their binding motifs. *BMC Genomics.* 16:649.
32. Renda, M., I. Baglivo, …, P. V. Pedone. 2007. Critical DNA binding interactions of the insulator protein CTCF: a small number of zinc fingers mediate strong binding, and a single finger-DNA interaction controls binding at imprinted loci. *J. Biol. Chem.* 282:33336–33345.
33. Filippova, G. N., S. Fagerlie, …, V. V. Lobanenkov. 1996. An exceptionally conserved transcriptional repressor, CTCF, employs different combinations of zinc fingers to bind diverged promoter sequences of avian and mammalian c-myc oncogenes. *Mol. Cell. Biol.* 16:2802–2813.
34. Xiao, T., P. Wongtrakoongate, …, G. Felsenfeld. 2015. CTCF recruits centromeric protein CENP-E to the pericentromeric/centromeric regions of chromosomes through unusual CTCF-binding sites. *Cell Reports.* 12:1704–1714.

35. Guo, Y., Q. Xu, …, Q. Wu. 2015. CRISPR inversion of CTCF sites alters genome topology and enhancer/promoter function. *Cell.* 162: 900–910.

36. Plasschaert, R. N., S. Vigneau, …, M. S. Bartolomei. 2014. CTCF binding site sequence differences are associated with unique regulatory and functional trends during embryonic stem cell differentiation. *Nucleic Acids Res.* 42:774–789.

37. Schmidt, D., P. C. Schwalie, …, D. T. Odom. 2012. Waves of retrotransposon expansion remodel genome organization and CTCF binding in multiple mammalian lineages. *Cell.* 148:335–348.

38. Shen, Y., F. Yue, …, B. Ren. 2012. A map of the *cis*-regulatory sequences in the mouse genome. *Nature.* 488:116–120.

39. Vietri Rudan, M., C. Barrington, …, S. Hadjur. 2015. Comparative Hi-C reveals that CTCF underlies evolution of chromosomal domain architecture. *Cell Reports.* 10:1297–1309.

40. Fudenberg, G., M. Imakaev, …, L. A. Mirny. 2016. Formation of chromosomal domains by loop extrusion. *Cell Reports.* 15:2038–2049.

41. Sanborn, A. L., S. S. P. Rao, …, E. L. Aiden. 2015. Chromatin extrusion explains key features of loop and domain formation in wild-type and engineered genomes. *Proc. Natl. Acad. Sci. USA.* 112:E6456–E6465.

42. Pope, B. D., T. Ryba, …, D. M. Gilbert. 2014. Topologically associating domains are stable units of replication-timing regulation. *Nature.* 515:402–405.

43. Shukla, S., E. Kavak, …, S. Oberdoerffer. 2011. CTCF-promoted RNA polymerase II pausing links DNA methylation to splicing. *Nature.* 479:74–79.

44. Burke, L. J., R. Zhang, …, R. Renkawitz. 2005. CTCF binding and higher order chromatin structure of the H19 locus are maintained in mitotic chromatin. *EMBO J.* 24:3291–3300.

45. Zuin, J., V. Franke, …, K. S. Wendt. 2014. A cohesin-independent role for NIPBL at promoters provides insights in CdLS. *PLoS Genet.* 10:e1004153.

46. Hayflick, L., and P. S. Moorhead. 1961. The serial cultivation of human diploid cell strains. *Exp. Cell Res.* 25:585–621.

47. Los, G. V., L. P. Encell, …, K. V. Wood. 2008. HaloTag: a novel protein labeling technology for cell imaging and protein analysis. *ACS Chem. Biol.* 3:373–382.

48. Efron, B., and R. J. Tibshirani. 1994. An Introduction to the Bootstrap. CRC Press, Boca Raton, FL.

Biophysical Journal, Volume *112*

Supplemental Information

Direct Observation of Cell-Cycle-Dependent Interactions between CTCF and Chromatin

Harsha Agarwal, Matthias Reisser, Celina Wortmann, and J. Christof M. Gebhardt

MATERIALS AND METHODS

Cell culture and cloning

We cultured WI-38 cells (Sigma-Aldrich, Steinheim, Germany) that carry a normal karyotype (1) in EMEM (Sigma-Aldrich, Steinheim, Germany) supplemented with 10% FBS (Sigma-Aldrich, Steinheim, Germany), 1% non-essential amino acids (Gibco by Life Technologies, Darmstadt, Germany) and 1% GlutaMax (Gibco by Life Technologies, Darmstadt, Germany). We generated a stable WI-38 cell line allowing for Doxycyclin (Dox)-inducible expression of CTCF, N-terminally fused to HaloTag (2) (Halo-CTCF), by inserting the plasmids for transactivator (pLenti-CMV-rtTA3, #26429, Addgene, Cambridge, USA) and Halo-CTCF using lentiviral transduction. To clone the vector containing Halo-CTCF, we used MultiSite Gateway technology (Invitrogen, Schwerte, Germany) with the two donor plasmids, pDONR 221 P1-P5r (Invitrogen, Schwerte, Germany) for N-terminal addition of HaloTag and pDONR221 P5-P2 (Invitrogen, Schwerte, Germany) for CTCF, both with flanking attB sites. The donor plasmids were cloned separately by BP clonase (Invitrogen, Schwerte, Germany) in order to perform site directed recombination. For HaloTag, flanked by attB1 and attB5 sites, we used the PCR primers fwd-primer: GGGGACAAGTTTGTACAAAAAAGCAGGCTTAATGGCAGAAATCGGTACTGGC and rev-primer: GGGGACAACTTTTGTATACAAAGTTGTGTTATCGCTCTGAAAGTACAGATCCTCAG. Similarly, we cloned the full length CTCF sequence with flanking attB5 and attB2 sites using the PCR primers fwd-primer: GGGGACAACTTTGTATACAAAAGTTGTAATGGAAGGTGATGCAGTCGAAG and rev-primer: GGGGACCACTTTGTACAAGAAAGCTGGGTTTCACTTGTCATCGTCATCTTTATAATCCCG. We combined the two donor vectors along with pLenti CMVTRE3G Puro Dest (# 27565, Addgene, Cambridge, USA) to obtain pLenti-CMVTRE3G-Puro-Halo-CTCF-Flag vector using LR clonase (Invitrogen, Schwerte, Germany). Cells were further sorted in a cell sorter (BD FACSAria III) to obtain cells expressing the Halo-CTCF construct.

Western Blot and flow cytometry analysis of CTCF expression

To analyze the expression of Halo-CTCF in our cell lines, we induced cells with different concentrations of Doxycycline 24 h before harvesting. For Western Blot, we lysed cells in RIPA buffer and determined the protein concentration with the Pierce BCA Protein Assay Kit (Thermo Fisher Scientific, Schwerte, Germany) by absorbance of the BCA/copper complex at 562 nm. We separated 12.8 µg of total protein by SDS-PAGE and transferred them to a nitrocellulose membrane (0.45 µm pore size). Antibodies used were anti-CTCF (rabbit monoclonal anti-CTCF, #ab128873, Abcam, Cambridge, UK) at 1:5000 and anti–α tubulin (rabbit monoclonal anti-α tubulin, #ab528665, Abcam, Cambridge, UK) at 1:50000. Detection was achieved with a

secondary anti-rabbit IgG (AP linked, #A3687, Sigma-Aldrich, Schnelldorf, Germany) at 1:30000 via chromogenic staining.
For flow cytometry analysis, we stained cells with HaloTag-SiR fluorescent ligand (provided by Kai Johnsson, EPFL) as described in the HaloTag protocol (Promega, Madison, USA), collected data on a FACSAria III system and processed it with the software FACSDiva 6.1.3.

Sample preparation

We seeded the cells on glass-bottom dishes (Delta T culture dishes, Bioptechs, Pennsylvania, USA) 2 days before the measurement. To induce the expression of Halo-CTCF, we added 5ng/ml doxycycline one day after cell seeding. To visualize the cells in G1, S and G2 phase, we added Premo FUCCI cell cycle sensor plasmids (Thermo Fisher Scientific, Schwerte, Germany) one day after cell seeding. We labelled the cells with HaloTag-SiR fluorescent ligand on the day of the experiment. Prior to some experiments, we stained DNA with 0.2 µg/ml Hoechst 33342 (Thermo Fisher Scientific, Schwerte, Germany) to identify cells in M phase. Single molecule imaging was performed in phenol free OptiMEM (Gibco by Life Technologies, Darmstadt, Germany) at 35 °C up to 120 min.

Single molecule fluorescence imaging and data acquisition

We performed single molecule fluorescence imaging on a custom built fluorescence microscope built around a commercial microscope body (TiE, Nikon, Tokyo, Japan). Four lasers were collimated, a 638 nm laser (IBEAM-SMART-640-S, 150 mW, Toptica, Gräfelfing, Germany), a 515 nm laser (Cobolt Jive 300 mW, Cobolt, Solna, Sweden), a 488 nm laser (IBEAM-SMART-488-S, 100 mW, Toptica, Gräfelfing, Germany) and a 405 nm laser (Laser MLD, 200 mW, Cobolt, Solna, Sweden) and combined using dichroic mirrors. Lasers were controlled by an AOTF (AOTFnC-400.650-TN, AA Optoelectronics, Orsay, France). We adjusted the laser beam with a pinhole and focused it on the back focal plane of a high-NA objective (100x 1.45 Plan Apo, Nikon, Tokyo, Japan) to achieve inclined illumination. For bright field illumination, we used a far red LED (660 nm, pE-100, 25W, CoolLed, Andover, UK). The emitted light was filtered by dichroic mirrors (F73-866 or F58-533, AHF, Tübingen, Germany), an emission filter (F72-866, AHF, Tübingen, Germany) and a notch filter (F40-072, AHF, Tübingen, Germany) before being detected by an EMCCD camera (iXon Ultra DU 897U, Andor, Belfast, UK). To control the setup, we used NIS Elements software (Nikon, Tokyo, Japan) and a NIDAQ data acquisition card (National Instruments, Austin, USA).
We fixed the camera integration time to 50 ms and varied the dark time between two consecutive frames in different time-lapse conditions for chromatin residence time measurements. For particle tracking measurements to determine the step distance distributions, we fixed the illumination time to 10 ms for two consecutive frame acquisitions, determined the step distance for these two

acquisitions, and inserted a 5 s dark time after each acquisition pair to allow for equilibration between diffusing and bound molecules.

Data analysis

Detection of molecules

Data analysis was performed in MATLAB (2014a, MathWorks, Natick, USA) as described previously (3). Briefly, single molecules were detected at a threshold of 4x standard deviation over the background and their positions were determined by a 2D Gaussian fit. Fluorescent molecules present in two consecutive frames within 0.5 to 1.5 pixels, dependent on the time-lapse time, were regarded as bound. Single molecule tracks separated by one frame in which the molecule was not detected were combined.

Determination of residence times

To extract residence times, defined as the inverse of a dissociation rate constant, we followed published protocols (3). We separated dissociation events of the labelled molecule from photobleaching events of the dye by recording movies with different time-lapse conditions. For each time-lapse condition, we compiled the times that a bound molecule was visible (fluorescent 'on' time) into a histogram (Fig. S5). Molecules whose fluorescent 'on' times were cut at the end of a movie were not counted, as this would disturb the analysis. We used a Levenberg-Marquardt least squares algorithm in Igor Pro (v.6.37, WaveMetrics, Portland, USA) to globally fit the histograms using decay models including a photobleaching rate constant and varying numbers of dissociation rate constants. The iterative fit terminated when the fractional decrease of χ^2 from one iteration to the next was less than 0.001 for nine iterations in a row. Based on the appearance of the plots of effective rate constants as function of time-lapse time (Fig. S5 and see below), we compared two models for the binding of Halo-CTCF to chromatin, a model with two dissociation rate constants:

$$f_2(t) = A \cdot \left[B \cdot \left(k_b \cdot \left(\frac{\tau_{on}}{\tau_{tl}} \right) + k_1 \right) \cdot \exp\left(- \left[k_b \cdot \left(\frac{\tau_{on}}{\tau_{tl}} \right) + k_1 \right] \cdot t \right) + (1 - B) \cdot \left(k_b \cdot \left(\frac{\tau_{on}}{\tau_{tl}} \right) + k_2 \right) \right. \quad (1)$$
$$\left. \cdot \exp\left(- \left[k_b \cdot \left(\frac{\tau_{on}}{\tau_{tl}} \right) + k_2 \right] \cdot t \right) \right]$$

and a model with three dissociation rate constants:

$$f_3(t) = A \cdot \left[B \cdot \left(k_b \cdot \left(\frac{\tau_{on}}{\tau_{tl}} \right) + k_1 \right) \cdot \exp\left(- \left[k_b \cdot \left(\frac{\tau_{on}}{\tau_{tl}} \right) + k_1 \right] \cdot t \right) + C \cdot \left(k_b \cdot \left(\frac{\tau_{on}}{\tau_{tl}} \right) + k_2 \right) \right. \quad (2)$$
$$\cdot \exp\left(- \left[k_b \cdot \left(\frac{\tau_{on}}{\tau_{tl}} \right) + k_2 \right] \cdot t \right) + (1 - B - C) \cdot \left(k_b \cdot \left(\frac{\tau_{on}}{\tau_{tl}} \right) + k_3 \right)$$
$$\left. \cdot \exp\left(- \left[k_b \cdot \left(\frac{\tau_{on}}{\tau_{tl}} \right) + k_3 \right] \cdot t \right) \right]$$

$f_2(t)$ and $f_3(t)$ represent the probability density of dissociation times. The global fit for both models included all fluorescent 'on' time histograms of all cell cycle phases. For Eq. 1, the parameters amplitude A, photobleaching constant k_b, dissociation rate constant k_1 and the fractions B and

$(1-B)$ were optimized during the fit. For Eq. 2, the parameters amplitude A, photobleaching constant k_b, dissociation rate constants k_1 and k_2 and the fractions B, C and $(1-B-C)$ were optimized during the fit. We allowed the dissociation rate constants and their amplitudes to be adjusted individually for each cell cycle phase, but the photobleaching rate constant was optimized globally for all phases. The parameters τ_{on} and τ_{tl} were pre-set. Since we could not resolve the smallest dissociation rate constant (k_2 in Eq. 1 and k_3 in Eq. 2) due to chromatin and cellular movements, we set its value to an upper bound of 0.001/s (Fig. S7). Table S1 summarizes the values for the dissociation rate constants and their amplitudes for the model with three dissociation rate constants, the photobleaching rate constant was (17.9 ± 0.8) /s in this case.

Determination of the number of dissociation rate constants

We define the effective rate constant k_{eff} of a fluorescent 'on' time histogram as the decay rate constant obtained from a fit with a single dissociation rate constant to the histogram:

$$f_1(t) = A \cdot\ k_{eff} \cdot \exp\left(-k_{eff} \cdot t\right) \tag{3}$$

In simulations of protein-DNA binding models we found that the effective rate constant as function of time-lapse time exhibits a minimum for each dissociation rate constant in the system, if the rate constants are well separated by approximately a factor of 10 or more (Fig. S6 A)(3). Thus, the effective rate constant as function of time-lapse time is a sensitive indicator of the number of dissociation rate constants present in the system. We therefore compared the effective rate constants extracted from the measured histograms with those extracted from histograms that were simulated with the parameters obtained from the global fits of Eqs. 1 or 2 to the measured histograms (Fig S6 B-D). The comparison yielded $\chi^2 = 0.51$ for two and $\chi^2 = 0.32$ for three dissociation rate constants. Due to the lower χ^2-value, we favor the model with three dissociation rate constants for CTCF-chromatin interactions over the model with two dissociation rate constants. Consistently, in a direct comparison of fit qualities, the reduced χ^2-value of the global fit with Eq. 2 (reduced $\chi^2 = 1.517$) is smaller than the value of the global fit with Eq. 1 (reduced $\chi^2 = 1.639$).

Determination of the bound fraction

In order to obtain the bound fractions of SiR-Halo-CTCF in G1, S and G2 phase, we determined the step distances of moving and bound molecules in two consecutively acquired frames and globally fitted the cumulative distribution functions of the particle's squared displacements by the function:

$$F\left(\frac{x^2+\ y^2}{4\tau_{tl}}\right) = A_1\left(1-exp\left(-\frac{x^2+\ y^2}{4D_1\tau_{tl}}\right)\right) + A_2\left(1-exp\left(-\frac{x^2+\ y^2}{4D_2\tau_{tl}}\right)\right) + (1-A_1 - A_2)\left(1-exp\left(-\frac{x^2+\ y^2}{4D_3\tau_{tl}}\right)\right) \tag{4}$$

where $D_i, i = 1,2,3$ denote the diffusion constants and A_1, A_2 and $(1 - A_1 - A_2)$ are the amplitudes. In this analysis, a slow apparent diffusion coefficient is observed which is due to the localization error of bound molecules. The corresponding amplitude thus represents the fraction of bound molecules (3). In order to avoid crossing paths, an upper limit of 8 pixels for the maximum squared displacement of a molecule was set. The last term of Eq. 4 was thus replaced by this limit using the function (3):

$$(1 - A_1 - A_2)\left(\exp\left(-\frac{x^2 + y^2}{4D_3\tau_{tl}}\right) - exp\left(-\frac{C_1}{D_3}\right)\right) / \left(\exp\left(-\frac{C_2}{D_3}\right) - exp\left(-\frac{C_1}{D_3}\right)\right)$$

where C_1 and C_2 are the constants denoting the upper and lower limits for the squared displacement of 0 and 8 pixels. The global fit included the distributions of all cell cycle phases. We allowed the amplitudes to be adjusted individually for each cell cycle phase, but the diffusion constants were optimized globally for all phases. Values for the bound fractions and errors were calculated by bootstrapping (4) as the mean and the standard deviation of parameters obtained from global fits to 2,000 random subsets of the displacements, each comprising 80% of the original data.

To estimate the fraction of CTCF molecules sporadically binding to chromatin in M phase, we compared the cumulative intensity of SiR-Halo-CTCF signal co-localizing with chromatin with the cumulative intensity of SiR-Halo-CTCF signal distributed around chromatin within a 15 s video. We repeated this measurement for 6 mitotic cells and computed the mean and standard deviation.

SUPPORTING FIGURES

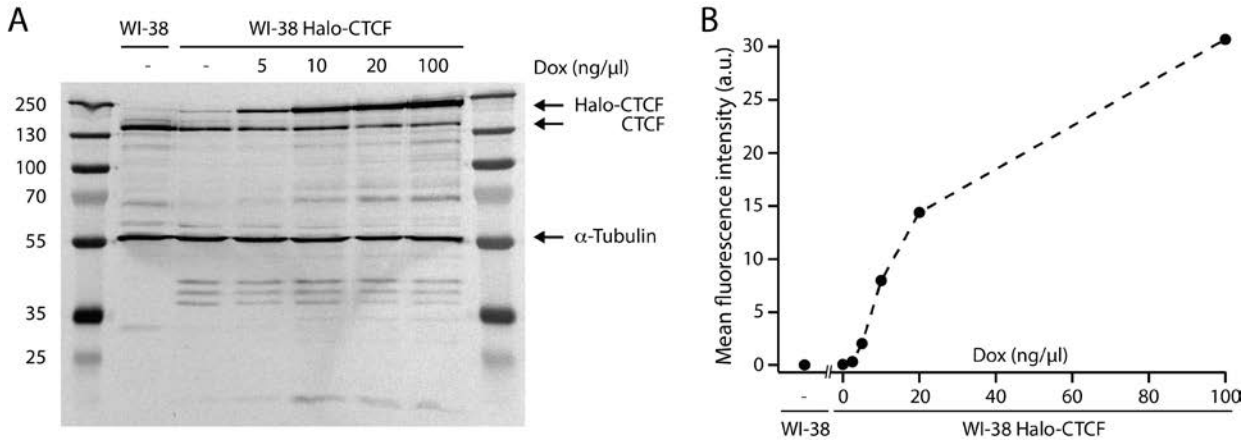

Fig. S1. Expression of Halo-CTCF in a stable WI-38 cell line. (**A**) Western Blot of CTCF and Halo-CTCF expression. Comparison of protein expression between WI-38 wild type cells and the WI-38 Halo-CTCF cell line, induced with the indicated concentrations of Doxycyclin. Lanes 1 and 8: PageRuler Plus Prestained Protein Ladder (Thermo Fisher Scientific, Schwerte, Germany). (**B**) Mean fluorescence intensity in flow cytometry measurements of cells without or with Halo-CTCF expression, labelled with HaloTag-SiR ligand, at different concentrations of Doxycyclin. The dashed line is a guide to the eye.

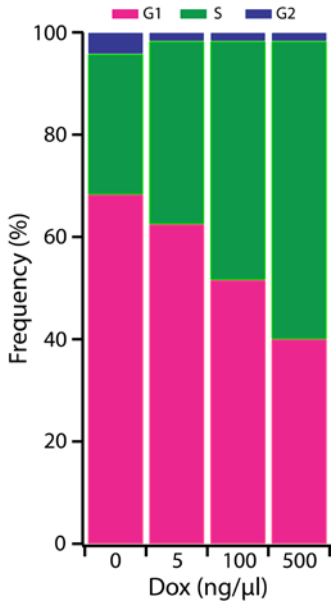

Fig. S2. Frequency of WI-38 Halo-CTCF cells in the different cell cycle phases G1 (magenta), S (green) and G2 (blue) at different concentrations of Doxycyclin (0 ng/µl: 120 cells, 5 ng/µl: 120 cells, 100 ng/µl: 120 cells, 500 ng/µl: 60 cells analyzed).

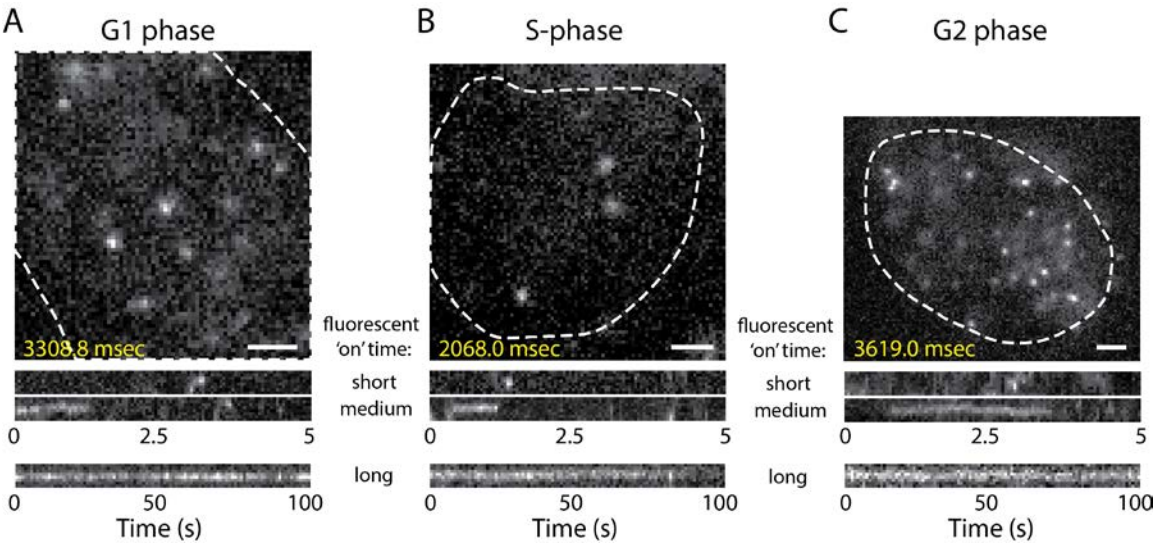

Fig. S3. Single molecule fluorescence imaging of SiR-Halo-CTCF in G1, S and G2 phase. Images of a WI-38 Halo-CTCF cell in (**A**) G1 phase (from Movie S2), (**B**) S phase (from Movie S3) and (**C**) G2 phase (from Movie S4) upon 638 nm laser excitation of SiR-Halo-CTCF at 50 ms camera integration time. The nucleus is depicted by the white dashed line. Scale bar is 2 µm. *Lower panels:* example kymographs of single molecules. The upper two kymographs are taken from the corresponding movies, the lower kymographs are taken from movies with 1 s time-lapse.

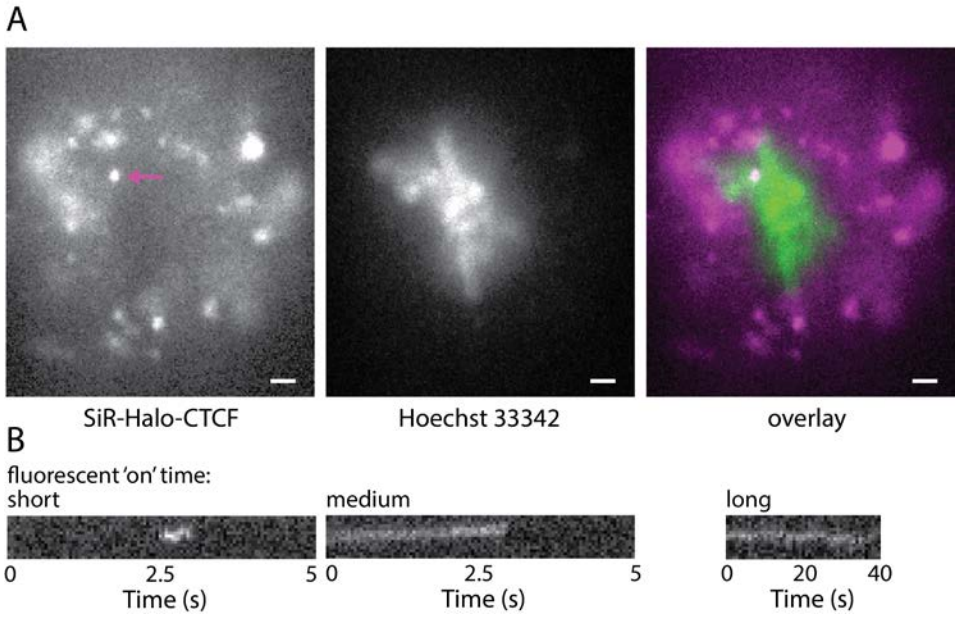

Fig. S4. Single molecule fluorescence imaging of SiR-Halo-CTCF in M phase. (**A**) Images of a WI-38 Halo-CTCF cell in M phase upon 638 nm laser excitation of SiR-Halo-CTCF (left, cumulative intensity of frames 1-55 of Movie S5), upon 405 nm laser excitation of Hoechst 33342 (middle) and overlay (right, magenta: SiR-Halo-CTCF, green: Hoechst 33342). Scale bar is 2 µm. (**B**) Example kymographs of single SiR-Halo-CTCF molecules co-localizing with the region stained by Hoechst 33342 (the middle kymograph is taken from Movie S5, the molecule highlighted in (A) by an arrow).

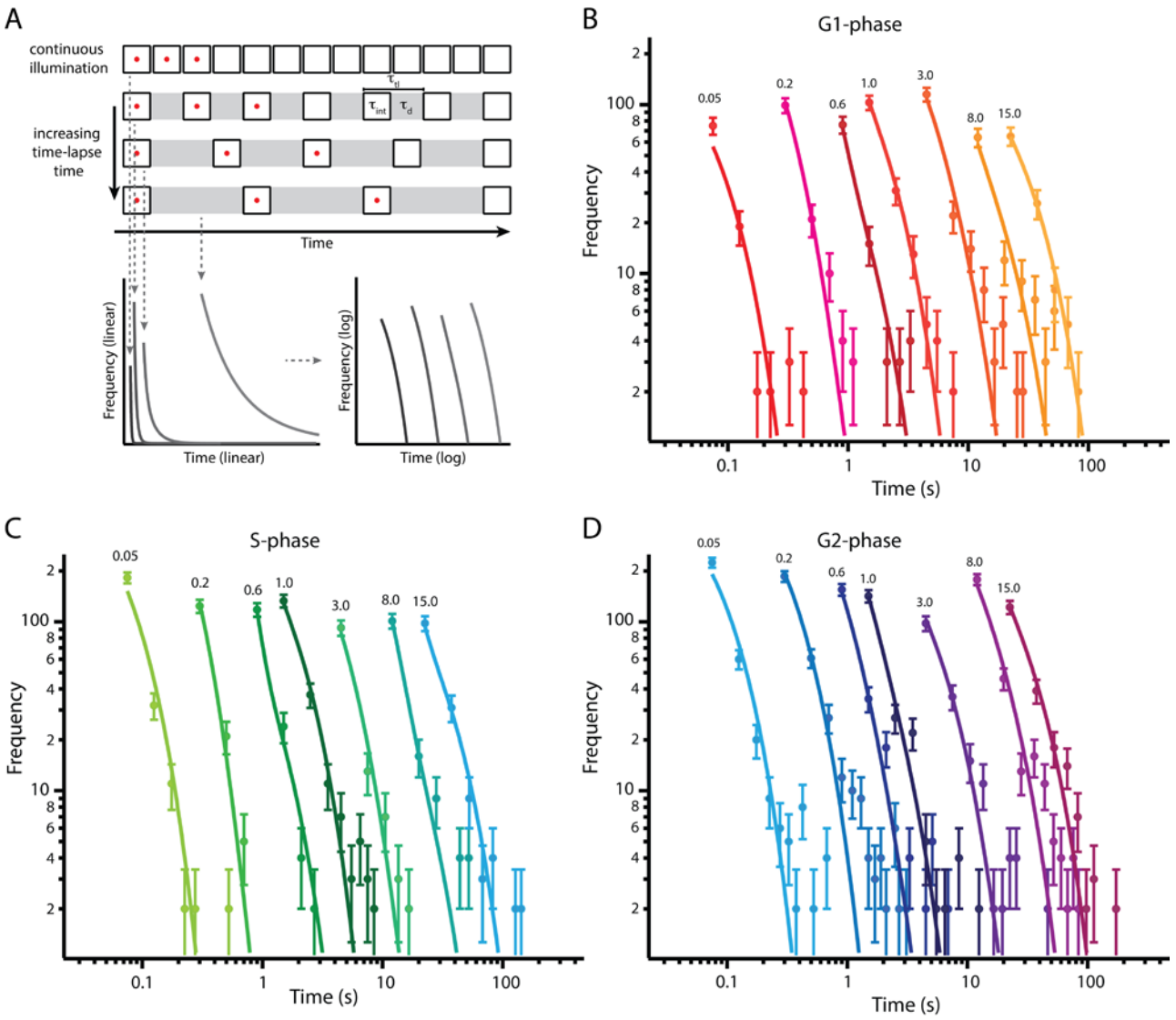

Fig. S5. Determination of chromatin binding times of SiR-Halo-CTCF. (**A**) Scheme of the time-lapse approach. Movies with camera integration time τ_{int} and differing dark time τ_d, both summing up to the time-lapse time τ_{tl}, are recorded. From movies with equal time-lapse condition, fluorescent 'on' times of SiR-Halo-CTCF molecules are extracted and compiled into a histogram. For better visualization, log-scales are chosen for both axes and bins with a single entry are omitted. (**B**-**D**) Histograms of fluorescent 'on' times (colored symbols) at different time-lapse times indicated by the number (in s) above each histogram, and at different cell cycle phases. (**B**) In G1 phase (n = 105 (τ_{tl} = 0.05 s); n = 141 (τ_{tl} = 0.20 s); n = 104 (τ_{tl} = 0.60 s); n = 160 (τ_{tl} = 1.00 s); n = 179 (τ_{tl} = 3.00 s); n = 105 (τ_{tl} = 8.00 s); n = 113 (τ_{tl} = 15.00 s); data from 11 cells). (**C**) In S phase (n = 236 (τ_{tl} = 0.05 s); n = 154 (τ_{tl} = 0.20 s); n = 151 (τ_{tl} = 0.60 s); n = 203 (τ_{tl} = 1.00 s); n = 123 (τ_{tl} = 3.00 s); n = 142 (τ_{tl} = 8.00 s); n = 150 (τ_{tl} = 15.00 s); data from 11 cells). (**D**) In G2 phase (n = 353 (τ_{tl} = 0.05 s); n = 336 (τ_{tl} = 0.20 s); n = 233 (τ_{tl} = 0.60 s); n = 215 (τ_{tl} = 1.00 s); n = 182 (τ_{tl} = 3.00 s); n = 286 (τ_{tl} = 8.00 s); n = 209 (τ_{tl} = 15.00 s); data from 9 cells). Lines are a global fit to all histograms from all cell cycle phases by an exponential decay model with three dissociation rate constants (Eq. 2 in Materials and Methods).

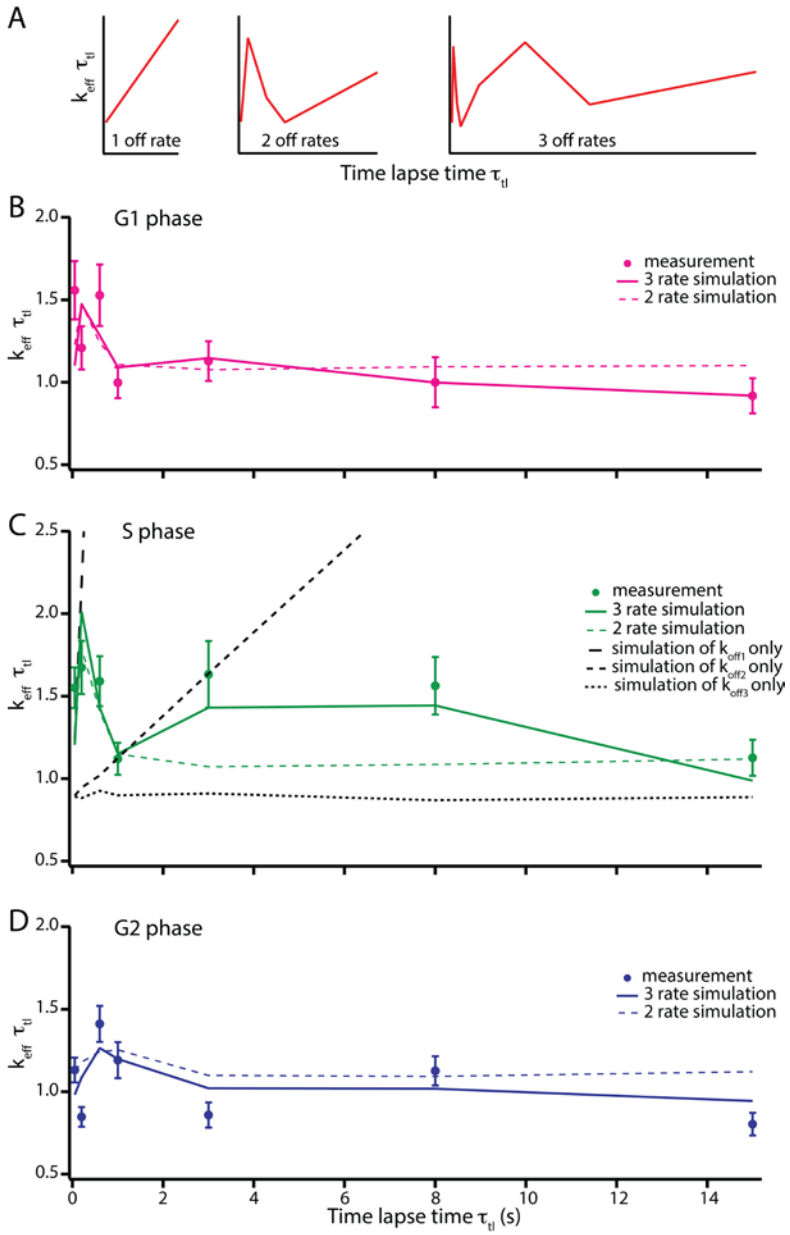

Fig. S6. SiR-Halo-CTCF exhibits three interaction states with chromatin. (**A**) Simulated plots of effective rate constants (k_{eff}) as function of time-lapse time (τ_{tl}) if one dissociation rate constant (left panel), two dissociation rate constants (middle panel) or three dissociation rate constants (right panel) are present in the system. Effective rate constants are obtained from a single exponential fit to a fluorescent 'on' time histogram of a certain time-lapse time (Eq. 3 in Materials and Methods). (**B**-**D**) Effective rate constant of SiR-Halo-CTCF as function of time-lapse time at different cell cycle phases extracted from measurements (symbols) and extracted from simulations of CTCF binding with two (dashed line) or three (continuous line) dissociation rate constants. Parameters of the simulations were obtained from global fits to all histograms from all cell cycle phases by an exponential decay model with two or three dissociation rate constants (Eqs. 1 and 2 in Materials and Methods). A comparison of measured with simulated effective rate constants for all cell cycle phases yielded $\chi^2 = 0.51$ for two and $\chi^2 = 0.32$ for three dissociation rate constants.

Error bars denote s.d. (**B**) Effective rate constant of SiR-Halo-CTCF as function of time-lapse time in G1 phase. (**C**) Effective rate constant of SiR-Halo-CTCF as function of time-lapse time in S phase. *Black lines:* Effective rate constants as function of time-lapse time extracted from simulations of CTCF binding if only dissociation rate constant k_{off1} (long dashed black line), only k_{off2} (short dashed black line) or only k_{off3} (dotted black line) were present. (**D**) Effective rate constant of Halo-CTCF as function of time-lapse time in G2 phase.

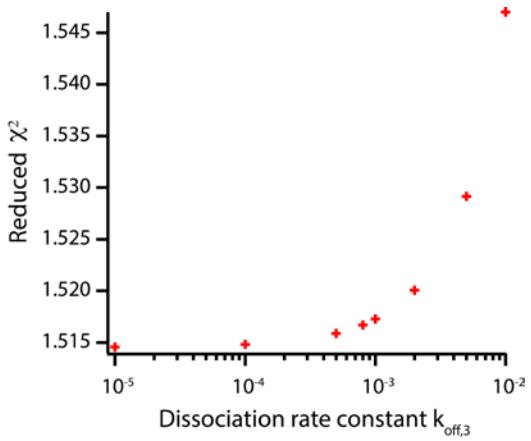

Fig. S7. Determination of an estimate for the dissociation rate constant k_{off3}. Reduced χ^2 values of a global fit with an exponential decay model with three dissociation rate constants (Eq. 2 in Materials and Methods) to fluorescent 'on' time histograms from all time-lapse conditions and all cell cycle phases as function of the dissociation rate constant k_{off3}. k_{off3} was held constant in each fit.

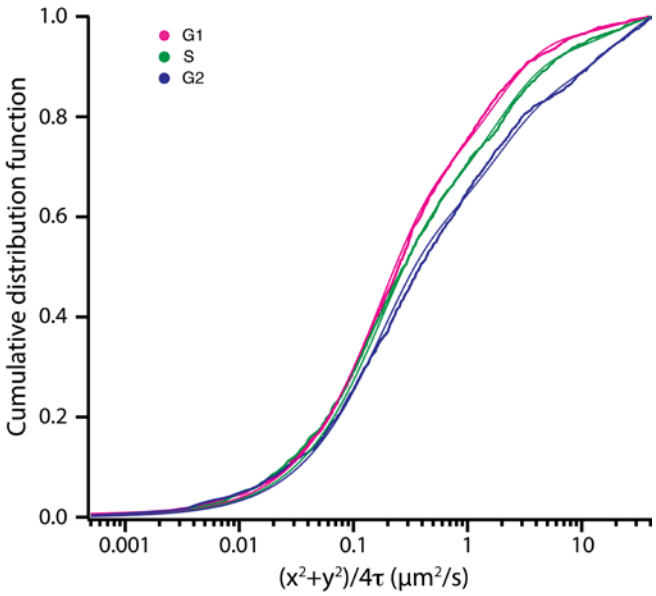

Fig. S8. Cumulative distribution functions of squared displacements of SiR-Halo-CTCF in G1 (magenta, *n* = 2097, 29 cells), S (green, *n* = 2397, 40 cells) and G2 phase (blue, *n* = 1759, 15 cells). Lines indicate a global fit with three effective diffusion components to the distributions (Eq. 4 in Materials and Methods).

SUPPORTING TABLE

Table S1: Binding times and fractions of SiR-Halo-CTCF binding to chromatin

	G1	S	G2	M
bound fraction	(54.6 ± 3.1) %	(52.1 ± 2.9) %	(48.1 ± 3.0) %	(0.008 ± 0.007) %
transient binding	(91.7 ± 5.6) % (0.23 ± 0.05) s	(98.7 ± 1.1) % (0.15 ± 0.02) s	(79.0 ± 9.6) % (0.63 ± 0.19) s	
dynamic binding	(5.8 ± 3.7) % (3.91 ± 1.47) s	(1.2 ± 1.0) % (4.08 ± 0.70) s	(10.4 ± 4.7) % (7.76 ± 4.46) s	
stable binding	(2.5 ± 1.9) % 1000 s	(0.1 ± 0.1) % 1000 s	(10.6 ± 4.9) % 1000 s	

Errors represent s.d.

SUPPORTING MOVIES

Movie S1. Control of SiR dye background. WI-38 cell not expressing Halo-CTCF after the labelling procedure for HaloTag-SiR fluorescent ligand including washing steps upon 638 nm laser excitation at 50 ms camera integration time.

Movie S2. SiR-Halo-CTCF in a WI-38 cell expressing Halo-CTCF in G1 phase upon 638 nm laser excitation at 50 ms camera integration time.

Movie S3. SiR-Halo-CTCF in a WI-38 cell expressing Halo-CTCF in S phase upon 638 nm laser excitation at 50 ms camera integration time.

Movie S4. SiR-Halo-CTCF in a WI-38 cell expressing Halo-CTCF in G2 phase upon 638 nm laser excitation at 50 ms camera integration time.

Movie S5. SiR-Halo-CTCF in a WI-38 cell expressing Halo-CTCF in M phase upon 638 nm laser excitation at 50 ms camera integration time.

SUPPORTING REFERENCES

1. Hayflick, L., and P.S. Moorhead. 1961. The serial cultivation of human diploid cell strains. Exp. Cell Res. 25: 585–621.
2. Los, G.V., L.P. Encell, …, K.V. Wood. 2008. HaloTag: A Novel Protein Labeling Technology for Cell Imaging and Protein Analysis. ACS Chem. Biol. 3: 373–382.
3. Gebhardt, J.C.M., D.M. Suter, …, X.S. Xie. 2013. Single-molecule imaging of transcription factor binding to DNA in live mammalian cells. Nat. Meth. 10: 421–426.
4. Efron, B., and R.J. Tibshirani. 1994. An Introduction to the Bootstrap. CRC Press.